Advances in Water Resources 51 (2013) 345–356

Contents lists available at SciVerse ScienceDirect

Advances in Water Resources

journal homepage: www.elsevier.com/locate/advwatres

A Raman lidar to measure water vapor in the atmospheric boundary layer

Martin Froidevaux [a], Chad W. Higgins [b,*], Valentin Simeonov [a], Pablo Ristori [c], Eric Pardyjak [d], Ilya Serikov [e], Ronald Calhoun [f], Hubert van den Bergh [a], Marc B. Parlange [a]

[a] School of Architecture, Civil and Environmental Engineering, Ecole Polytechnique Fédérale de Lausanne (EPFL), Switzerland
[b] Department of Biological and Ecological Engineering, Oregon State University, Corvallis, United States
[c] CEILAP (CITEFA-CONICET), Zufriategui, Argentina
[d] Department of Mechanical Engineering, University of Utah, Salt Lake City, United States
[e] Max-Planck-Institut für Meteorologie, Hamburg, Germany
[f] Arizona State University, Tempe, United States

ARTICLE INFO

Article history:
Available online 8 May 2012

Keywords:
Atmospheric boundary layer
Raman lidar
Water vapor

ABSTRACT

A new multi-telescope scanning Raman lidar designed to measure the water vapor mixing ratio in the atmospheric boundary layer for a complete diurnal cycle with high resolution spatial (1.25 m) and temporal (1 s) resolutions is presented. The high resolution allows detailed measurements of the lower atmosphere and offers new opportunities for evaporation and boundary layer research, atmospheric profiling and visualization. This lidar utilizes a multi-telescope design that provides for an operational range with a nearly constant signal-to-noise ratio, which allows for statistical investigations of atmospheric turbulence. This new generation ground-based water vapor Raman lidar is described, and first observations from the Turbulent Atmospheric Boundary Layer Experiment (TABLE) are presented. Direct comparison with in-situ point measurements obtained during the field campaign demonstrate the ability of the lidar to reliably measure the water vapor mixing ratio. Horizontal measurements taken with time are used to determine the geometric characteristics of coherent structures. Vertical scans are used to visualize nocturnal jet features, layered structures within a stably stratified atmosphere and the internal boundary layer structure over a lake.

1. Introduction

The development of new instrumentation to probe the spatial characteristics of the atmospheric boundary layer (ABL) is paramount to improving our understanding of land-atmosphere exchange over complex terrain [44,16–18]. The variability of the earth's surface with respect to topography, surface roughness, soil moisture distribution, and land use impact the various scales of motion in the turbulent ABL, and the resulting local transport of heat, water vapor, and momentum. While fast response point sensors have become standard in the micrometeorological community due to their relatively reliable and robust operation [37], measurements of the spatial variability of atmospheric turbulence over field scales, on the order of 500 m, has remained less well developed. Arrays of sonic anemometers have been used to obtain spatially resolved measurements of turbulence quantities with typical array sizes limited to 10s of meters [53,59,49,34,29,33,5]. These spatial data sets have proven invaluable for a priori understanding subgrid scale physics for Large-Eddy Simulation (LES), but lack the full range of spatial scales resolved by LES.

High resolution numerical approaches such as LES have been used to simulate the interactions of the land surface with the atmosphere over complex terrain [57,47,3,39,64,69,13]. These simulations require land surface boundary and atmospheric initial conditions [2], as well as new means of validation. Thus, there remains an obvious requirement for measurement tools that can temporally and spatially resolve the multiple atmospheric scales responsible for the transport of heat, water vapor and momentum at the land-atmosphere interface.

The use of range resolved remote sensors (e.g. sodar, lidar, radar) over the past decades in atmospheric research has had a significant impact on our knowledge of the boundary layer, e.g. [42,11,40,55,4,9,12,21,36,46]. These devices have been used to gain tremendous insight into various processes in the atmospheric boundary layer (e.g. entrainment, dispersion, etc.) as well as particular quantities in the atmospheric boundary layer that have been traditionally difficult to measure (e.g. boundary layer heights, inversion depths, etc.) [68]. However, these techniques are still limited to relatively large spatial and temporal resolutions. Two historically competing lidar technologies for remote sensing of water vapor are the DIAL (differential absorption of light) and

* Corresponding author. Address: 116 Gilmore Hall, Corvallis, OR 97331, United States.
E-mail address: chad.higgins@oregonstate.edu (C.W. Higgins).

0309-1708/$ - see front matter © 2012 Elsevier Ltd. All rights reserved.
http://dx.doi.org/10.1016/j.advwatres.2012.04.008

Raman lidars [27]. DIAL lidars utilize a combination of particle and molecule scatter, while Raman lidars operate on a principle based solely on scatter from molecules [68]. The advantages and disadvantages of the techniques have been reviewed by Grant [27].

The Raman lidar approach to measure water vapor in the atmosphere was initially proposed in the late 1960s [38,10], but its development was limited due technical difficulties such as unstable laser sources, inadequate data acquisition systems, and eye safety restrictions. The renewed interest in the Raman lidar technique for water vapor measurements was kindled by the results presented in Melfi and Whiteman [41] and Vaughan et al. [62]. The main advantage of the Raman lidar approach, compared to other approaches, is that the laser source does not have to be tuned to a specific water vapor absorption line [27]. Additionally, Raman lidar allows for the high spatial and temporal resolution that is necessary to study the turbulent atmosphere boundary layer dynamics. The Raman lidar technique is now well established as an advanced research tool in the atmospheric sciences [50,35,67,48,26,61,60,66,14,30,17]. Limitations such as low spatial and temporal resolution, day-time operation, and signal attenuation with range ($1/r^2$) where r is distance from the laser source) have led to the limited use of Raman lidars in micrometeorology. Solutions for day-time operation have been proposed by Renaut and Pourny [50], Goldsmith et al. [26] and have been used to guide our design.

In this paper we present a new ground-based scanning Raman lidar designed to measure the water vapor mixing ratio at high spatial (1.25 m) and temporal (1 s) resolution over a range of up to 500 m at near constant signal-to-noise ratio (SNR). A description of the field deployment, validation of the instrument, and first observations are presented. We show that the Raman lidar can be used to identify and characterize features of the atmospheric boundary layer that have traditionally been difficult to measure including: advected coherent structures, the impact of the nocturnal jet, layering resulting from stable atmosphere stratification, and internal boundary layer formation at land surface transitions.

2. EPFL high resolution Raman lidar

The EPFL (Ecole Polytechnique Fédérale de Lausanne) instrument is a solar-blind, scanning Raman lidar. The lidar was designed to measure water vapor mixing ratio during the day and night with raw spatial and time resolutions of 1.25 m and 1 s respectively. The primary design challenges arise due to the demanding temporal and spatial resolution requirements with almost constant accuracy within the range of 15–500 m. The novel, multi-telescope design of the lidar, (see Appendix for more details) allows for water vapor profiling with almost constant measurement error over the whole operational range. By contrast, the measurement error of conventional lidars increases quadratically with the measurement range. Daytime operation is achieved by using UV wavelengths shorter than 300 nm which fall within the 'solar blind' region of the electromagnetic spectra, thus ensuring that daylight has a minimal

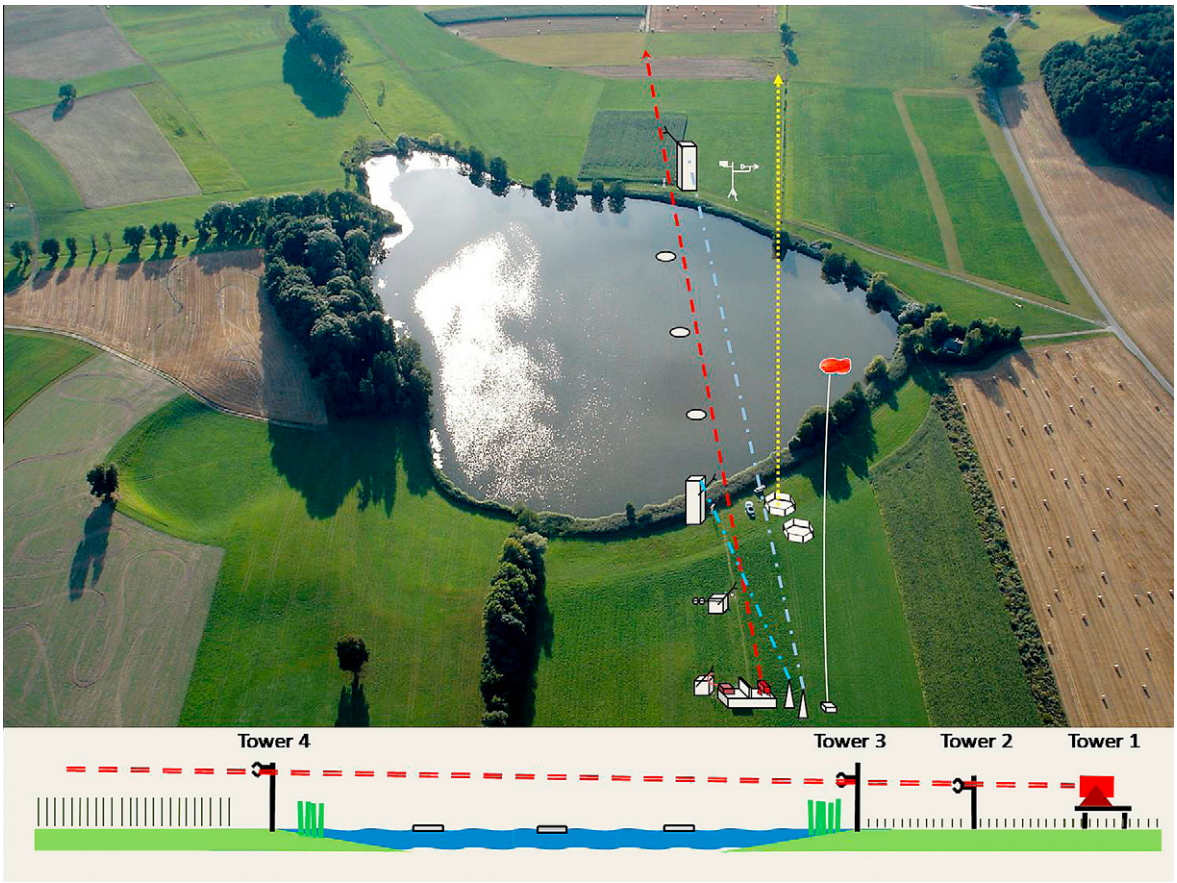

Fig. 1. (Top panel) Aerial photograph of the lake and experimental setup looking toward the west, and (bottom panel) side view schematic of the experiment showing the path of the lidar beam (red dashed line) relative to the surface and instruments. The vertical line of sight of the sodar is indicated by the dashed yellow line. The white disks on the lake surface represent the hobo sensors used to measure the lake surface temperature. Two sciltillometers were deployed along the blue dashed lines and a tethered balloon provided profiles of humidity and temperature (not used in the present analysis).

effect on the measurements. Azimuthal and elevation scanning with a resolution of 1° and scanning speeds up to 6°/min allow for observation of a hemisphere centered on the laser light source.

Some of the technical advances made to overcome these challenges are discussed in the detailed description given in the Appendix.

3. TABLE-08

The TABLE-08 (Turbulent Atmospheric Boundary Layer Experiment) was carried out during the month of August 2008 in Seedorf (FR/Switzerland) around and above a small lake (46.78444°N, 7.04083°E). The objective of the TABLE-08 field experiment was

Table 1
TABLE-08 Sensors summary.

Instruments sites	Height [m]	Range [m]	Measured variables	Sensor type	Sampling rate	Accuracy
LIDAR		15–600	MR	Ro-vibrational Raman	1 s	±0.3 g/kg
			T	Pure-rotational Raman	1 s	Unknown
SODAR/RASS		30–400	*u*, *v*, *w*	MFASScintec	15 mn	±0.1, 0.1, 0.05 m/s
			Tv	RASSScintec	15 mn	±0.2 °K
Balloon		0–200	*P*, *alt*	SW35	1–5 s	±0.5 hPa, ±0.5 m
			Tdew, *T*	SW35withSRS-C34	1–5 s	±0.1∼K, ±0.2∼K
Tower 1	2.50		*u*, *v*, *w*, *Tv*	Ultrasonic anemometer	20 Hz	±1, 1, 0.5 mm/s, ±0.002 °K
			q, CO_2	Open-path analyser	20 Hz	±0.26, ±0.01 mmol/m^3
			N_2O, CH_4, H_2O, CO_2	Quantum cascade laser	10 Hz	Unknown
Tower 2	2.50		*u*, *v*, *w*, *Tv*	Ultrasonic anemometer	20 Hz	±1, 1,0.5 mm/s, ±0.002 °K
			q, CO_2	Open-path analyser	20 Hz	±0.26, ±0.01 mmol/m^3
			RH (2x), *T* (3x)	Capacitive, Pt100, TC	5 s	±1%, ±0.2 °K, ±0.2 °K
			P, *Tsurf*	P Transducer, IRgun	1 mn	±0.5 hPa, ±0.3 °K
			wdir, *wspeed*	Wind vane, cup	1 mn	±2°, ±0.1 m/s
			SW (up/dw) LW (up/dw)	Radiometers	1 mn	± 2%, ±3%
			tG	Thermopile	1 mn	±b%
Tower 3	4.34		*u*, *v*, *w*, *Tv*	Ultrasonic anemometer	20 Hz	±1, 1, 0.5 mm/s, ±0.002 °K
			q, CO_2	Open-path analyser	20 Hz	±0.2b, ±0.01 mmol/m^3
			RH, *T*	Capacitive, Pt100	5 s	±1%, ±0.2 °K
			H, Ct2	SLS	1–5 mn	Unknown
			Soil ψ, soil *T*, soil θ	Ceramic, thermistor, dielectric	2 mn	±5 kPa, ±1 °K, ±2%
Tower 4	7.07		*u*, *v*, *w*, *Tv*	Ultrasonic anemometer	20 Hz	±1, 1, 0.5 mm/s, ±0.002 °K
			q, CO_2	Open-path analyser	20 Hz	±0.26, ±0.01 mmol/m^3
			RH, *T*	capacitive, Pt100	5 s	±1%, ±0.2 °K
			P, *Tsurf*	P Transducer, IRgun	1 mn	±0.5 hPa, ±0.5 °K
			H, Ct2	Scintillometer	5 mn	Unknown
			Rain	Rain gauge	2 mn	±10%
			Rn, *wdir*, *wspeed*	Pyranometer, anemometer	2 mn	±5%, ±7%, ±l m/s
			RH, *T*	Capacitive, thermistor	2 mn	±3%, ±0.5 °K
LAKE	0.00		water *T*	Thermistor	5 s	±0.2 °K
	0.00		water *T*	Thermistor	5 s	±0.2 °K
	0.00		water *T* (3x)	Thermistor	5 s	±0.2 °K

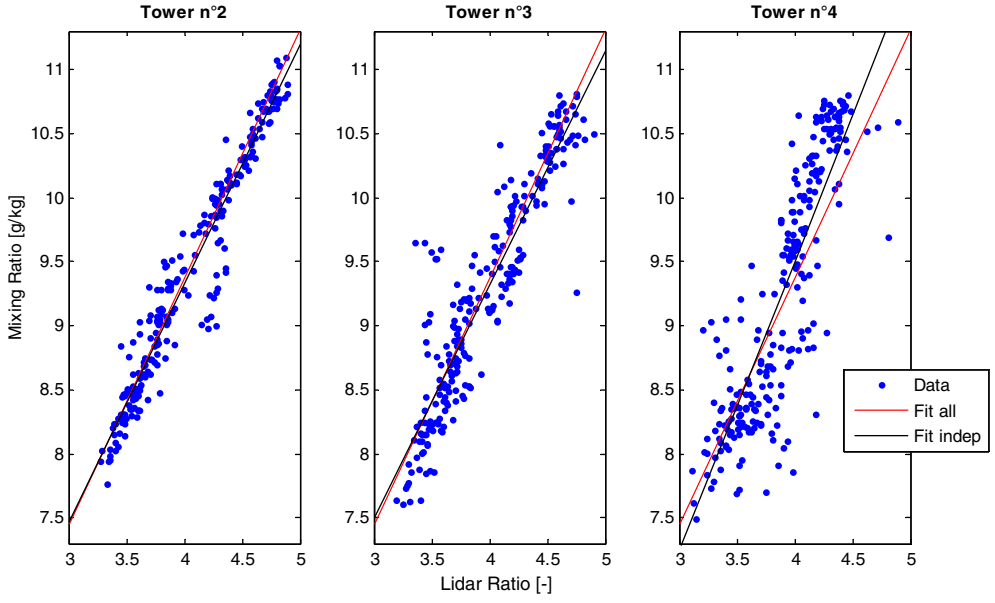

Fig. 2. Lidar mixing ratio calibration curves at the three towers (60, 135 and 513 m) during TABLE-08.

to validate the EPFL high resolution Raman lidar and to study the effects of the lake on the local microclimate.

The site is located on the Swiss plateau at a drained peat bog that has been converted into productive agriculture fields. The field is surrounded by hills that extend ~120 m above the valley floor toward the North and South. A lake, in the center on this small valley, is fed mainly by ground water contributions. The lake is about 400 m wide and is surrounded by tall grass, creating a rough transition between the water and the surrounding agriculture fields. Fig. 1 is a photograph of the lake looking toward the West showing the instrumental setup and the state of vegetation during the field campaign. A profile of the terrain running along the lidar beam path is sketched at the bottom of the figure. Horizontal lidar measurements were taken with a small inclination of 1.5° to ensure eye safety. With this configuration, the laser beam was at heights of 2.5, 4.34 and 7.07 m above ground respectively at towers 2, 3 and 4. Thus, the lidar beam passed within ~30 cm of the sensors mounted on each tower where the water vapor mixing ratio was measured with two different techniques: LICOR LI7500 fast response infrared gas analyzer and calibrated slow response Rotronic XB temperature relative humidity sensors. Tower 2 was also instrumented to measure the surface energy budget, including fully resolved radiation balance, soil heat flux, and sensible/latent heat flux measurements. A sodar/RASS system, providing vertical profiles of wind speed, wind direction and virtual temperature, was installed close the lake edge. A tethered balloon equipped with a Meteolabor "Snow-White" chilled mirror dewpoint hygrometer to measure temperature and humidity was used for atmospheric profiling from ground level to 150 m (height limited by civil and military aviation security). The lake surface temperature was also monitored with HOBO TidBit v2 thermometers attached to the bottom of Styrofoam flotation devices at three locations, aligned under the laser beam. The complete description of the TABLE-08 instrumental setup with measured variables, sensor types, sampling rates and accuracies is summarized in Table 1.

3.1. Verifying the lidar performance

Data with a signal-to-noise ratio less than 5 were rejected. Also known as the Rose criterion, it is the SNR needed to distinguish image features with 100% certainty [8]. A sensitivity analysis was performed to determine the effect of temporal averaging on the maximum range of the instrument (defined as the range where the SNR drops below 5). As expected, longer averaging times

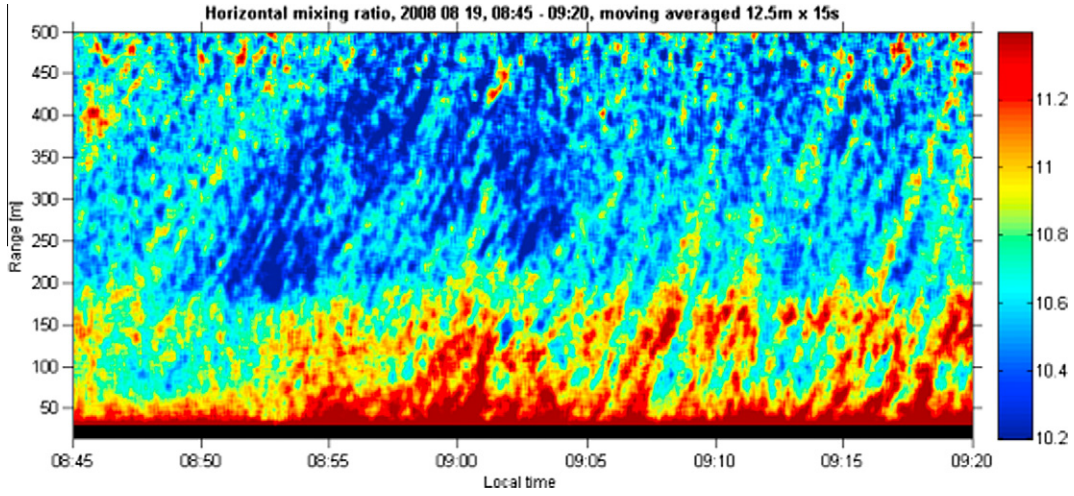

Fig. 3. Contour plot of the mixing ratio during a horizontal scan (TABLE-08, 19 August 2008 08). The wind blows from the lidar (0 m) to the lake (150–500 m), entraining water vapor from the grass field (0–150 m).

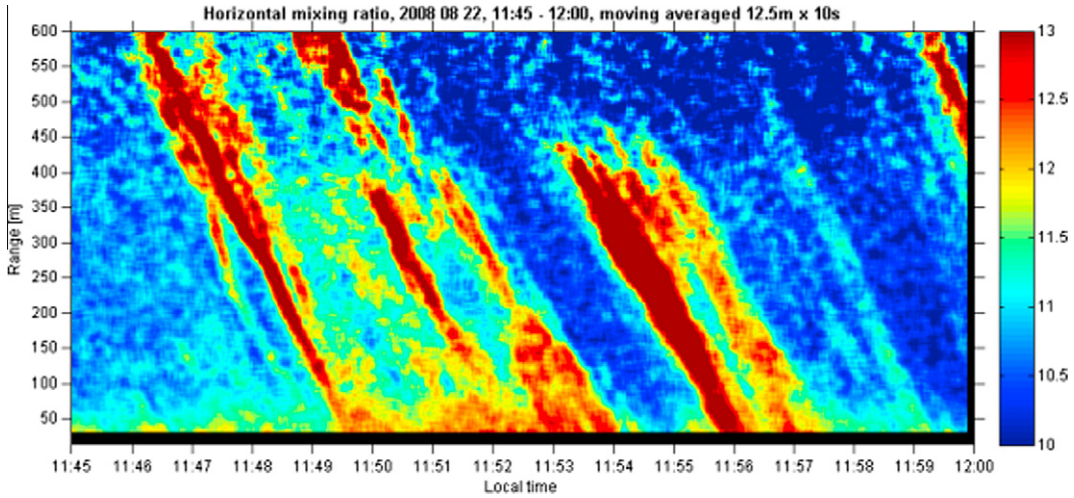

Fig. 4. Horizontal lidar scan showing the mixing ratio evolution on 22 August 2008. Large persistent flow features of humid air masses crossing the entire lidar observation range can be observed. In this figure the prevailing wind direction is toward the lidar (from 600 m to 0 m).

resulted in a greater effective range of the instrument; however, the range reached an absolute maximum at 1200 m where additional averaging no longer extended the range. The proximity of the horizontal staring position of the laser beam to the tower's sensors allowed for assessment of the lidar calibration at three different points. Ideally, a single calibration should apply if the multi-telescopes lidar design is suitable for accurate measurements of water vapor over the entire measurement range. Two minute averages of the water vapor mixing ratio from the towers were compared to the ratio of water vapor to nitrogen Raman scattering obtained from the lidar over the same time interval. The lidar signal was then averaged over three bins, corresponding to 3.75 m. To obtain a proper calibration, a wide range of absolute water vapor mixing ratio values are needed; for this purpose, 18 h of measurements over three days are used (20, 22, and 25 August 2008) with mixing ratios ranging from 7.5 to 11 g of water vapor per kilogram of dry air. The calibration constants are computed for the three different ranges, 60, 135 and 513 m, each tower independently or the three combined (Fig. 2). The maximum deviation for the range independent calibration, computed with a least squared linear regression, was ~5% with the largest error at tower 4. The best calibration function considering the three towers simultaneously is given by:

$$MR_{lidar} = 1.888\frac{S_{H_2O}}{S_{N_2}} + 1.993 \quad (1)$$

In Eq. (1), MR_{lidar} is the lidar retrieved water vapor mixing ratio in g/kg$_{dry}$, S_{H2O} and S_{N2} are the baseline corrected rotational-vibrational Raman signals from water vapor and nitrogen, respectively. The comparison is excellent with R^2 values of 0.946, 0.862 and 0.726 at the three different ranges from the lidar and for 2 min averaging of the signal. The measurement accuracies, defined as the standard deviation of the difference between both types of measurements are 0.16, 0.23 and 0.32 g/kg$_{dry\ air}$ for towers 2, 3 and 4, respectively. At ambient temperature, a shift of 0.3 g/kg$_{dry\ air}$ in the mixing ratio corresponds to approximately 1.7% relative humidity. A comparison of variances and spectra given by the lidar and LICOR7500 was also performed and presented in [28].

3.2. Horizontal observations

Valuable insight into the flow structures passing over the lake can be obtained when the lidar is pointed horizontally at a fixed height and the mixing ratio is measured along the beam in time. Figs. 3 and 4 show a contour plot from this type of experiment. Numerous diagonal stripes are observed in the time-space-mixing ratio graphs. Such water vapor signatures are visible during most daytime horizontal sounding periods at the TABLE-08 site. Two measurement periods where horizontal measurements are taken are shown; one with the wind blowing from the lidar to the lake (Fig. 3), and a second with the wind blowing across the lake toward the lidar (Fig. 4). Note that in both figures, the air above the land surface has a higher water vapor mixing ratio. This is expected in the daytime as the land surface is much warmer than the lake surface and the land surface has an actively transpiring crop of clover. Also in both figures, persistent flow features are visible independent of wind direction, and support the idea that such humidity patterns are not specific to certain surface roughness properties

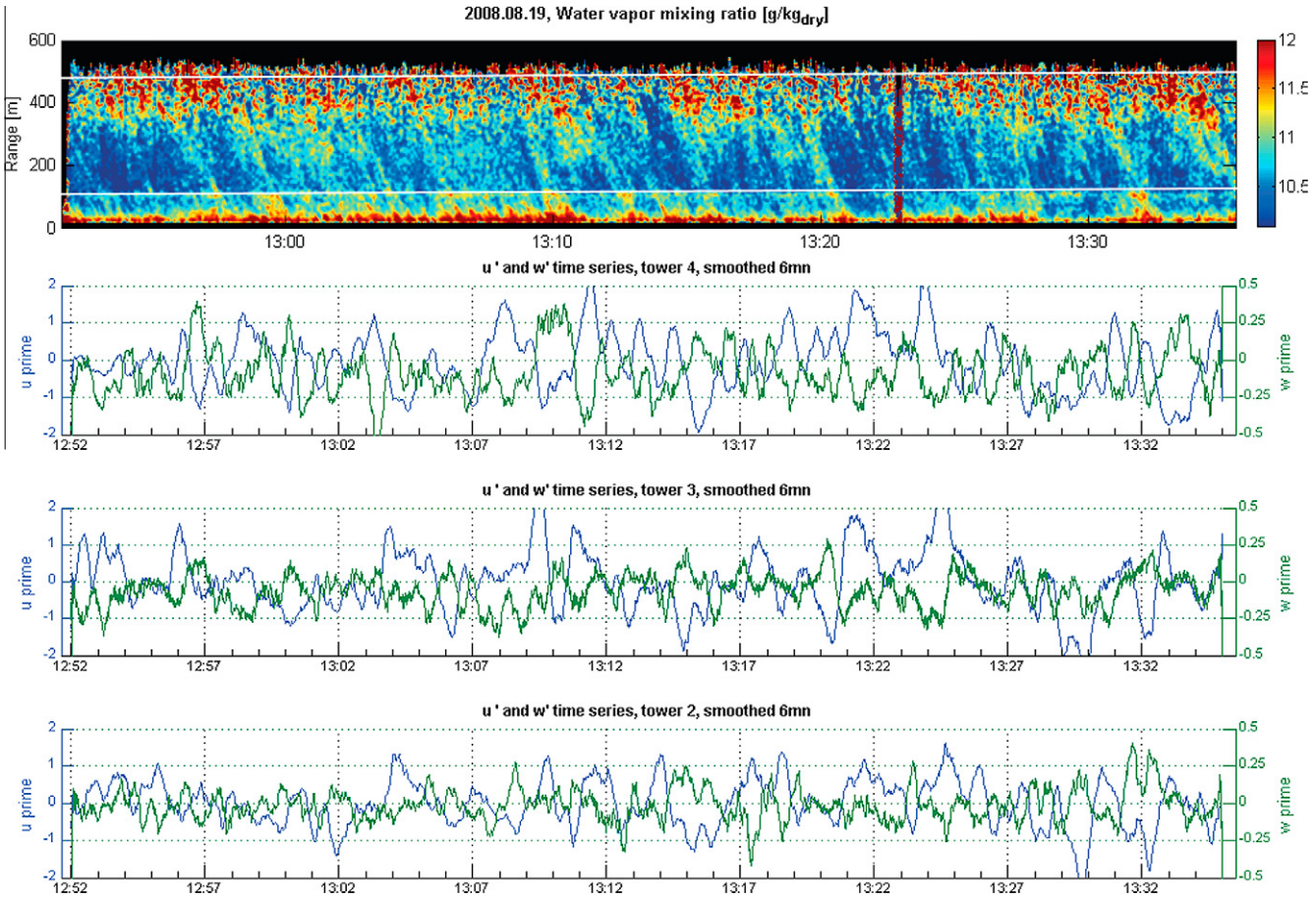

Fig. 5. time series of the fluctuating stream-wise and vertical velocity components shown with the corresponding lidar humidity image. White lines on the upper panel represent the positions of towers 3 and 4 (122 m and 486 m respectively) at the edges of the lake.

(e.g., corn field, harvested weeds, fallows, clovers and trees) but are more universal.

The persistent flow features were first analyzed by correlating the observed velocity vectors with the advected humidity structures in an attempt to tease out the underlying physical mechanisms. In such a case, relationships between the humidity structures observed with the lidar, and the wind vector components measured by ultrasonic anemometers are expected. Furthermore, patterns in the velocity signal are expected to advect across the experimental transect with the humid structures. A time series of the lidar humidity data is presented alongside the fluctuating velocity components at each tower in Fig. 5. Regions with a SNR < 5 are displayed in black. The relationship between the lidar data and these wind patterns is not obvious. Ejection and sweep events do not correspond exactly in time to higher values of mixing ratio lidar measurements, and there is no clear pattern that is advected from one tower to another. For example, the two largest wind events at tower 3 (135 m in the time–space lidar plot), correspond to a high humidity event (13:09) and a low humidity event (13:23) respectively.

Since no clear pattern emerged from the analysis of wind vector components, a geometric approach was adopted. With this approach, each coherent humidity structure is identified and analyzed according to the approach summarized in Fig. 6(a). In Fig. 6(a), a plan view of a portion of the beam is sketched. The blue box represents a coherent structure, which enters the beam at a certain time ($t3$) and range ($r3$). The wind advects this structure up to a point where it completely crosses the lidar beam (central light blue box), and until it finally leaves the beam (last light blue box). The extent of an individual structure along the beam ($r1$ and $r2$) and the propagation time ($t3$ ant $t4$) can be determined directly from the lidar data. Combining this information with the wind speed, and the angle of the wind with respect to the laser beam orientation, the span-wise dimension of this coherent signature W is retrieved. The stream-wise dimension L is obtained by taking the distance along the beam when the structure enters and leaves the sounding beam ($r3$ and $r4$). This simple method is applied to the calibration days (20, 22, and 25 August 2008), corresponding to 18 h of measurements, where 137 structures have been quantified. Histograms of the stream-wise and span-wise extent of the coherent structures determined from the above analysis are presented in Fig. 6(b) and (c) respectively. The major result of this analysis is that the stream-wise extent of these structures, in the direction of the wind, is approximately two times larger than the span-wise extent. Thus, these coherent structures could be imagined as elongated patterns of moisture, which are consistent with nested packets of hairpin vortices [1]. The existence of self-organizing vortices in the mixed layer is still subject to study in the atmospheric boundary layer community [19,24]. Numerical simulations have been used to reproduce and understand such structures, with DNS (i.e. [31,63,54]) or LES (i.e. [57,47,39,64,69,13]). Observations of such structures have been obtained in wind tunnel facilities [6,32,43,20]. Previous studies of vortex organization in the turbulent boundary layer with Particle Image Velocimetry (PIV), have shown that hairpin vortex signatures populate the boundary layer abundantly [1], and the conceptual representation they give seems to be the best match to the phenomena observed with the lidar. Such bended tubes with heads up and the tails close to the ground induce low speed fluid cores from near the surface. This could explain why coherent signatures of humidity have been measured at different heights over the entire lidar measurements range and over different roughness transitions. Still, one may ask the question, is the humidity observed in the field consistent with an organized nested packet of hairpin vortices? One hypothesis is that, due to its smaller density, water vapor is taken from the ground and concentrated in the induced low speed fluid core of the hairpin packet. To our knowledge, it is the first time that such complete structures have been measured systematically in the space-time domain with water vapor Raman lidar at field scales.

3.3. Vertical scans

The scanning ability of the EPFL Raman lidar allows for different visualizations of the atmosphere compared to a static orientation.

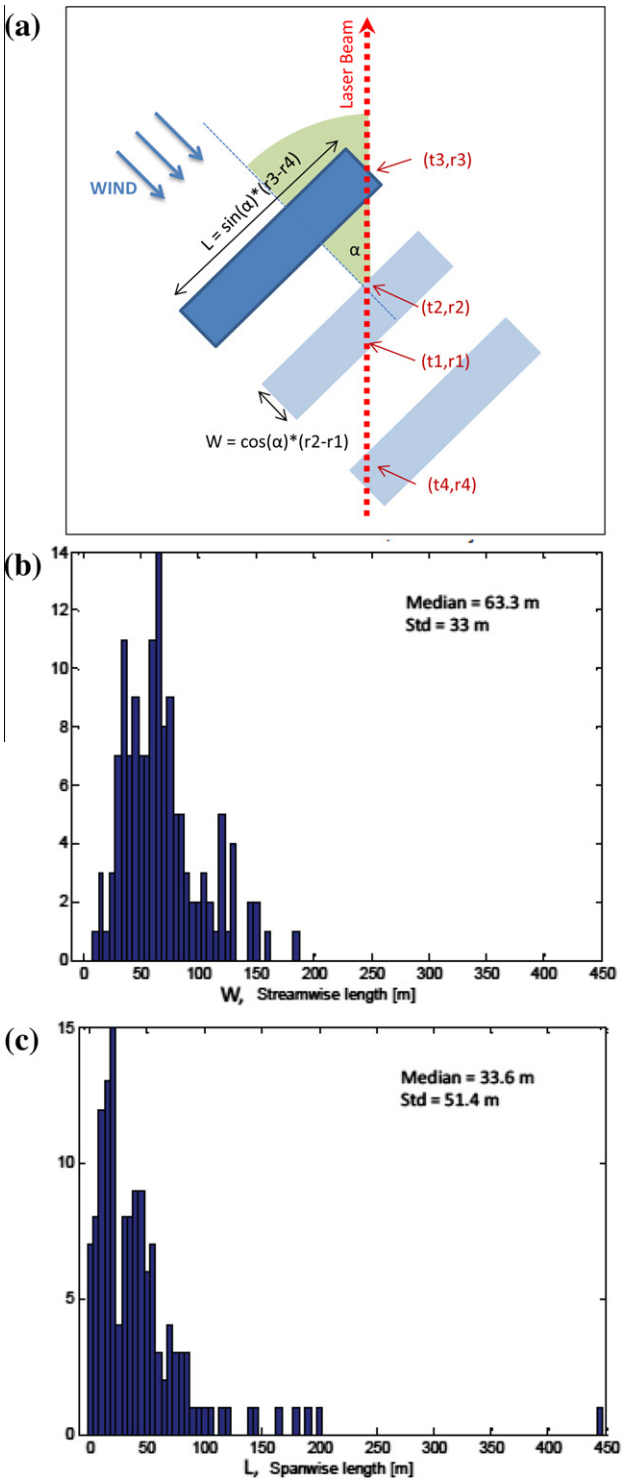

Fig. 6. (a) Schematic of the coherent structure geometry analysis principle. (b) A histogram of the streamwise size of the coherent structures, and (c) a histogram of the cross-stream size of the structures.

Three vertical scans are presented below, which demonstrate three types of atmospheric boundary layer phenomena: a nocturnal jet, a multi-layered stable atmosphere, and an internal boundary layer that develops above Seedorf lake. Each colored contour plot represents the distance-altitude-mixing ratio concentration measured with Raman lidar during one scan. The experimental setup with the wind direction and wind speed measured at 2.5 m above ground are sketched at the top of each of the panels in Figs. 7–9.

3.4. Nocturnal jet

This lidar vertical downward scan (Fig. 7), taken during the TABLE-08 field campaign was recorded from 02:03 to 02:20 CET on the 30th of August 2008. The small black dots at the bottom part of the scan are inconsistent values due to fog scattering. Two profiles of horizontal wind speed, wind direction, vertical wind speed and virtual potential temperature measured by the sodar/RASS during the scan interval time are shown on the right. The vertical lidar scan shows a less humid layer of air between 200 and 350 m, which corresponds to a nocturnal jet with a maximum speed of 7 m/s centered at 280 m. At low altitude, a strong change of wind direction is visible in the sodar data and is related to the lowest visible humidity layer on the lidar scan, at about 40 m above ground. The virtual potential temperature profile from the RASS, does not completely match the water vapor layers.

3.5. Multilayered stable atmosphere

Fig. 8 shows an example of a stably stratified and layered atmosphere. It is a downward vertical scan, acquired between 21:10 and 21:31 CET on the 29th of August 2008. Three mean vertical profiles are extracted from this scan and presented in the right panel of Fig. 8. The blue line is a vertical profile taken above the grass field upwind of the lake, the green line corresponds to the middle part of the experiment above the lake and the red line was obtained just downwind of the lake. These

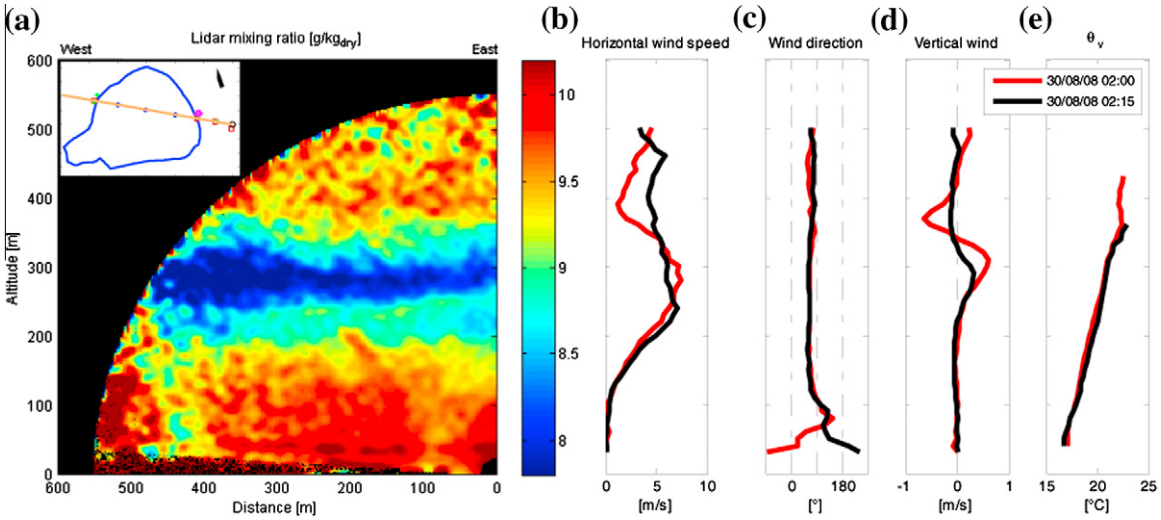

Fig. 7. (a) Vertical lidar scan taken between 02:03 to 02:20 CET with profiles of wind speed (b), wind direction (c), vertical wind (d) and virtual potential temperature (e) Profiles were measured with the Sodar–Rass instrument at 2:00 CET (red line) and 2:15 CET (black line). The black points at the bottom part of the lidar scan in (a) are due to fog scattering. The nocturnal jet at about 280 m produces a distinct layer of dry air. At this time, the Obukhov length was 4.6 m measured at tower 2 (height of measurement 2.47 m). The vapor pressure deficit measured at tower 2 was 0 hPa, consistent with the formation of fog.

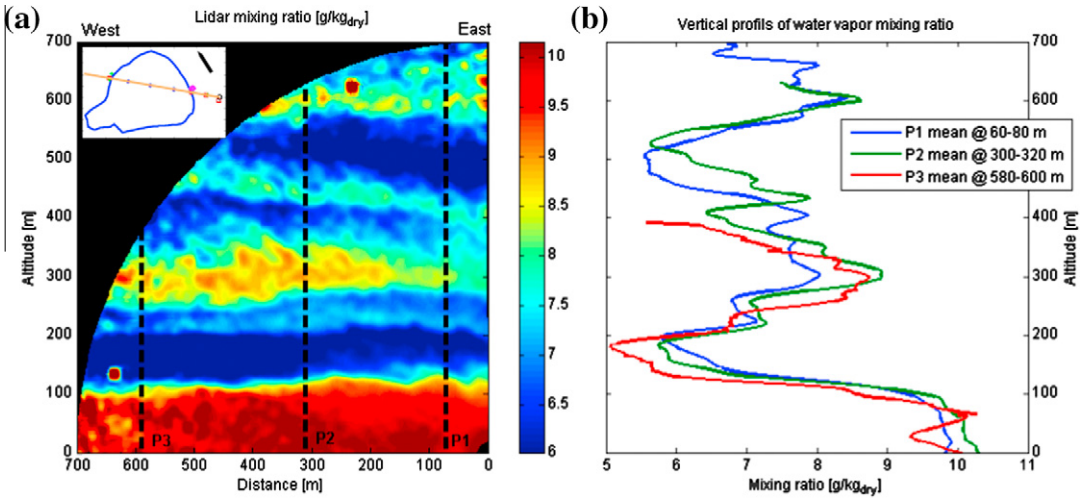

Fig. 8. (a) Vertical lidar scan taken between 21:10 and 21:30 CET on the 29th of august, and three extracted profiles (b). The profiles were extracted from the lidar scan at the locations indicated by the vertical dashed lines. The 100 first meters of the ABL exhibits large water vapor concentration where the internal boundary layer from the lake is slightly visible. Numerous water vapor layers are visible above the lake. At this time, the Obukhov length was 2.7 m measured at tower 2 (height of measurement 2.47 m). The vapor pressure deficit measured at tower 2 was 2.7 hPa.

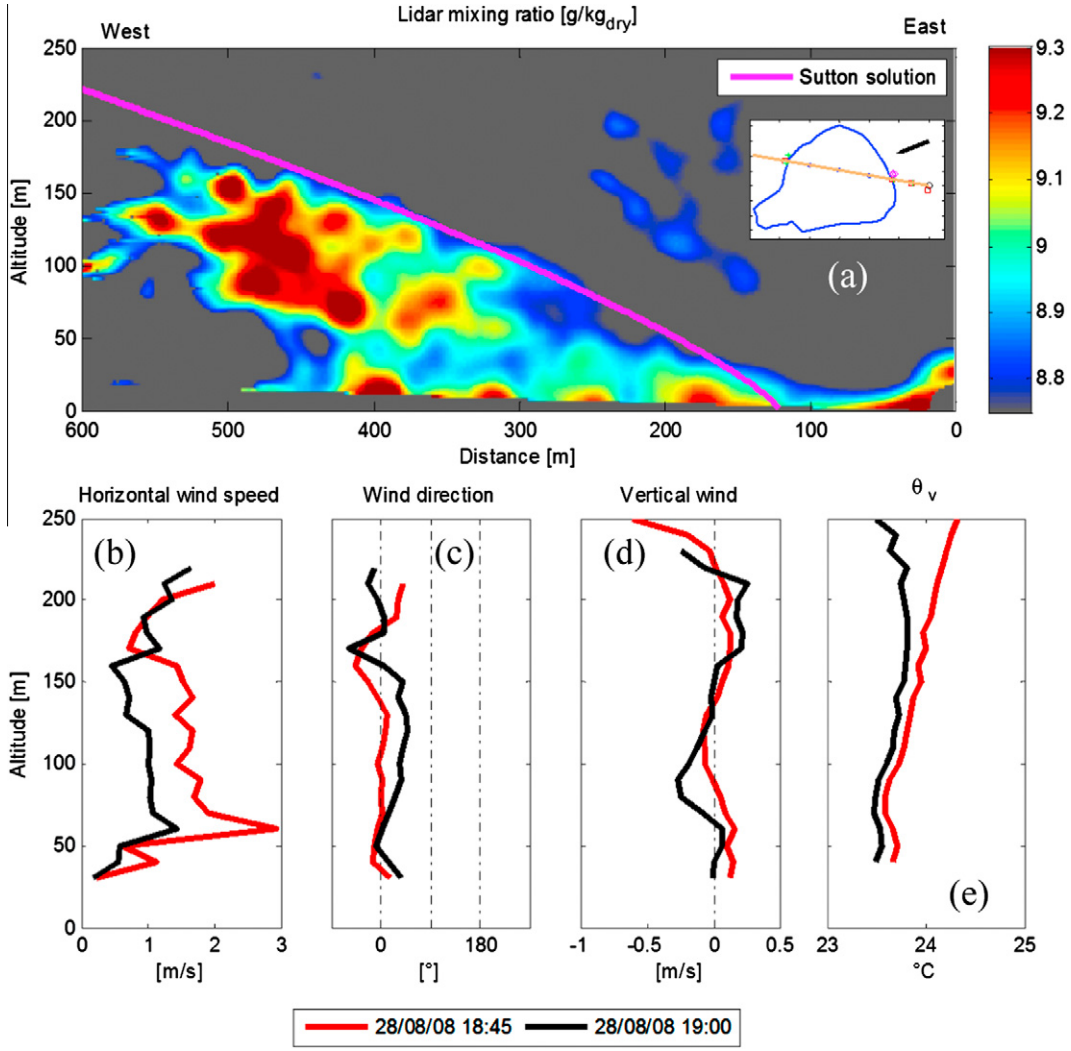

Fig. 9. (a) Plot of water vapor mixing ratio from a vertical scan illustrating the existence of a moist internal boundary layer. The lidar scan was taken between 18:31 and 18:53 CET on august 28th 2008. Profiles from the Sodar–Rass are presented of wind speed (b), wind direction (c), vertical winds (d), and potential temperature (e). The Sutton solution is shown in pink. At this time, the Obukhov length was −2.8 m measured at tower 2 (height of measurement 2.47 m). The vapor pressure deficit at tower 2 was 17 hPa.

extracted profiles illustrate the multi-scale behavior a stably stratified atmosphere above the lake. There are three main layers, surrounded by smaller secondary layers, which are in turn surrounded be even smaller tertiary layers. This layering occurred during one of the most stable episodes observed over the land surface with $z/L = 0.91$ measured at tower 2, where L is the Obukhov length. In the same vertical lidar scan, the internal boundary layer of the lake, located within the first layer, can be also seen. This observation is partially confirmed by the shape of the first 100 m from the three vertical extracted profiles (Fig. 8). The wind at 2.5 m above ground, measured with the cup and vane anemometer, is southeasterly blowing across the lake. Thus, the first extracted profile should not be influenced by the presence of the lake. The second profile was taken above the lake and exhibits higher mixing ratios; likely due to the lake water vapor transfer. Finally the third profile, taken downwind, shows a similar mixing ratio value at the ground as the one taken before the lake. This last profile has a peak at ~70 m, corresponding to the lake's water vapor internal boundary layer extent. The presence of an internal boundary layer is expected at this time, as the lake surface temperature was greater than the surrounding land surface and air temperature.

3.6. Lake internal boundary layer

The behavior of the development of internal boundary layers (IBLs) in the atmosphere associated with the horizontal advection of air across discontinuities is a subject of great interest and one in which there is still a great deal of scientific uncertainty [25]. The EPFL Raman lidar provides a tool to investigate the spatial and temporal details of humidity with IBLs [45]. Fig. 9 shows the lowest portion of a 90° vertical lidar scan looking downwind from the lidar, measured from 18:31 to 18:53 CET on the 28th of August 2008. The time required to scan the lower region near the ground, which included the IBL, was approximately 6 min. Simultaneous wind and temperature profile measurements from the sodar/RASS are presented below the lidar scan. As illustrated by the virtual potential temperature profiles shown in Fig. 9, the atmosphere during the scan was stable above ~75 m. In the figure, the lake is located between 140 and 480 m. In the presented case, the discontinuities of the land surface are: roughness changes (from agriculture field to water surface with tall grass along the edge of the lake), temperature changes (from vegetated soil to water) and of course humidity (from land surface to open water). Different mathematical descriptions have been proposed in the literature for the different

types of internal boundary layers as a function of the surface propriety changes. For example, [58] developed an analytical approach to describe the IBL development over a step change in near-surface humidity, from relatively dry to wet surfaces. His theory was further expanded by [23] and is discussed in detail by Brutsaert [7]. The key assumptions are steady horizontal wind and negligible variation of mean velocities in the vertical and lateral directions leading to a balance between horizontal advection and divergence of the vertical turbulent flux of water vapor in the mean water vapor budget. This leads to the following equation, which describes the thickness of the internal boundary layer of the water vapor as a function of along-wind fetch x:

$$\delta_v = cx^{(2+m-n)^{-1}}. \quad (2)$$

Here, $m = 1/7$ and $n = 1 - m$ for neutral stability flows, $c = 1.82$, and x is the direction along the land surface aligned with the mean wind and $x = 0$ is the dry to wet interface position. Eq. (2) is plotted on Fig. 9, and shows excellent agreement with the observed internal boundary layer. It is interesting to note that this internal boundary layer was captured at about 18:50, and appeared right after the change of stability regime over the land, from unstable to stable.

4. Conclusion

The goal of this paper was to validate the multi-telescope design of the EPFL Raman lidar and to evaluate the ability of this instrument to measure water vapor mixing ratio and land-atmosphere exchange. The lidar-point sensor comparison performed during the TABLE-08 field campaign demonstrates the ability of the lidar to accurately measure the water vapor mixing ratio, and validates its multi-telescope design. The accuracy of the water vapor mixing ratio is better than 0.32 g kg^{-1} of dry air, when compared signals averaged over 2 min and a height increment of 3.75 m along the laser beam. The horizontal measurements of water vapor coherent structures, their analysis and the corresponding eddy covariance data allow us to claim that such patterns are consistent with the expected geometry of the cores of nested packets of hairpin vortices. It is, to our knowledge, the first time that such structures have been measured with a Raman lidar.

The scanning capability and the high temporal and spatial resolution of this Raman lidar offer a broad range of potential applications. The vertical scans give information about the extent of layers and boundary layer structures. Evidence of strong relationships between low-level jets and the water vapor distribution in the air have been observed. The multi-scale layering of the stable boundary layer has been described. The humid internal boundary layer over the lake has been also measured successfully. This study demonstrates the ability of a state-of-the-art Raman lidar to measure land-atmosphere interactions and offers a promising new tool and understanding of the atmospheric boundary layer.

Acknowledgements

The authors gratefully acknowledge funding from the Swiss Science Foundation and the NCCR MICS (Mobile Information Communications Systems).

Appendix A

A.1. Water vapor Raman lidar

A lidar (LIght Detection And Ranging) is a laser-based, optical instrument, which allows remote profiling of atmospheric parameters such as aerosol backscatter, humidity, temperature, gas concentration, wind speed and direction [65]. A lidar transmits short laser pulses into the atmosphere and detects and analyzes the backscattered light from the atmosphere. This backscattered light contains information on atmospheric properties. The range to a scattering volume is determined by measuring the time between the transmission of the laser pulse and the detection of the backscattered radiation. Since the length of the instantly probed air volume is proportional to the laser pulse duration, the latter determines the profile range resolution.

The power of the backscattered light $P(r)$ is proportional to the transmitted laser power P_0, telescope surface area A, and instrumental efficiency η and depends on the backscatter coefficient $\beta(r)$ and atmospheric transmission $T(r)$ through the so called scattering lidar equation:

$$P(r) = P_0 \frac{A}{r^2} \ln \beta(r) T^2(r), \quad (A.1)$$

where r is the along beam distance, $l = c\tau/2$ is the spatial resolution (depth of the scattering volume), c is the speed of light, and τ the laser pulse duration.

In the special case of inelastic light-matter interaction, known as Raman scattering, the backscatter coefficient is proportional to the number density of the scattering molecules. The scattered wavelength differs from the laser wavelength and is specific for each scattering compound. These properties of Raman scattering are used in Raman lidars for water vapor mixing ratio measurements. The water vapor profile $q(r)$ is derived from the ratio of water vapor $P_{H2O}(r)$ to nitrogen $P_{N2}(r)$ Raman signals as:

$$q(r) = k \frac{P_{H_2O}(r) T_{N_2}(r)}{P_{N_2}(r) T_{H_2O}(r)} \Gamma(r), \quad (A.2)$$

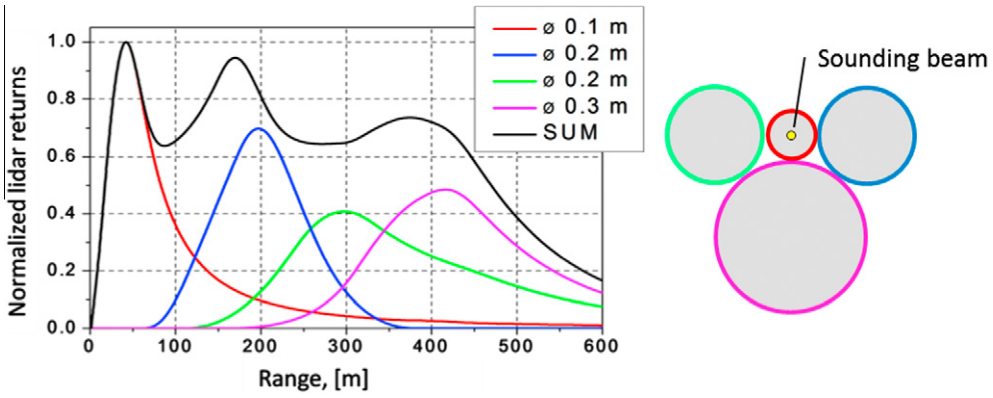

Fig. A.1. (Left) Individual and total normalized lidar return signal, and (right) illustration of the four-telescope design with mirrors of diameters 0.1, 0.2, and 0.3 m.

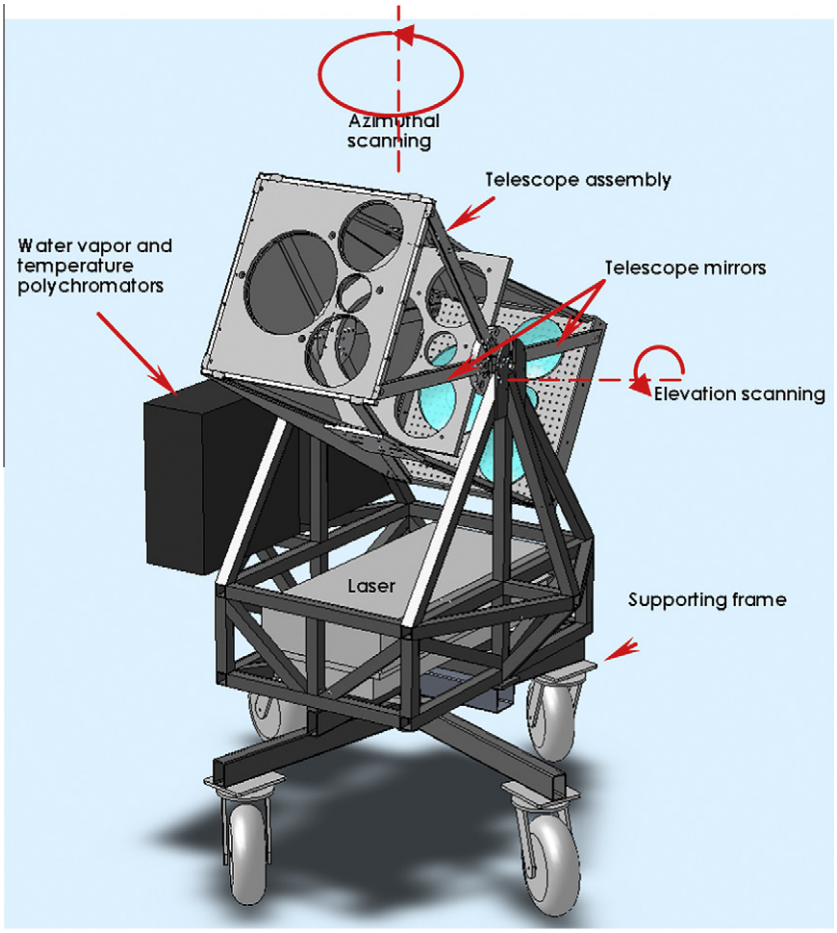

Fig. A.2. 3D projection of the EPFL Raman lidar.

where k is a calibration coefficient determined by comparison with a reference instrument. The ratio $T_{N2}(r)/T_{H2O}(r)$ accounts for the difference in the atmospheric transmission at the water vapor and nitrogen Raman wavelengths due particle scattering which can be neglected in under clear atmospheric conditions. $\Gamma(r)$ is a correction function for the difference in the atmospheric transmission due to molecular scattering and absorption. At laser wavelengths longer than 320 nm, the main contribution to $\Gamma(R)$ is due to Rayleigh scattering by air molecules and can be calculated precisely from pressure profiles. At shorter wavelengths the differences in the ozone absorption have to be taken into account. The ozone correction can be estimated from the average ozone concentration, measured independently [15] or by using an additional Raman signal [50].

The majority of the existing Raman lidars are built with the goal to cover the largest possible part of the troposphere. Raman lidars allow measurements up to the stratosphere during the nighttime and up to the mid troposphere during the day. Typical spatial resolutions for such systems are from tens of meters, to hundreds of meters. The time resolution could be from minutes, close to the lidar, to hours at longer distances see [50,35,67,48,26,61,60,66,14,30]. The only lidar with high spatial and temporal resolution, designed for short measurement distances, apart from the described here EPFL system, is the lidar described in [15,16,18,45].

A.2. EPFL Raman lidar

Since solar background in the visible spectrum is much greater than any Raman scattering, the EPFL lidar operates in the UV spectral band, known as the "solar-blind" region (wavelengths shorter than 300 nm), where nearly all solar radiation is absorbed by stratospheric ozone [50]. Therefore, the lidar transmitter uses a quadrupled Nd:YAG laser, emitting 40 mJ pulses at 266 nm with pulse duration of 4 ns and repetition rate of 100 Hz.

A novel "multi-telescope" array, designed to reduce the native high dynamic range of the lidar signals caused by the inherent $1/r^2$ dependence (see Eq. (A1)), is used in the lidar receiver. The array consists of four parabolic mirrors with diameters of 10, 20, 20, and 30 cm. The signals from the individual mirrors are summed optically to form a composite signal. The telescope sizes and their orientation with respect to the laser beam have been selected so that the intensity variation due to the range dependence of the composite signal is lower than 60% from 50 to 500 m as shown in Fig. A.1 [52,56,51]. The small dynamic range of the composite signal yields nearly constant statistical error with constant temporal and spatial resolution over the entire operational range of the lidar while also helping to minimize the errors caused in the analog-to-digital conversion of the signals.

To simplify the optical scheme used for summing, the light from each telescope is delivered by optical fiber to the spectral unit used to separate the individual Raman signals. Dichroic beam-splitters, installed in front of each fiber, reflect light with a wavelength shorter than 274 nm, thus preventing systematic errors due to fluorescence in the optical fibers caused by the strong backscatter at the laser wavelength. This reflected short-wavelength radiation, contains pure Rotational lines of nitrogen and oxygen, and will be used for temperature measurements, now in development. The final wavelength separation of water, nitrogen, and oxygen Raman signals is performed by a prism- based polychromator. The oxygen

channel is used to correct for the difference in the atmospheric transmission caused by tropospheric ozone at water vapor and nitrogen wavelengths (see Eq. (A.2)). The optical signals are detected in analog mode by photomultiplier tubes and acquired by eight channel 14 bit, 120 MHz ADC.

To allow for the observation of a wide range of ABL phenomena, the lidar has full-hemisphere scanning abilities. The elevation scanning is performed by rotating the telescope array around a horizontal axis. The laser beam is delivered along this axis by a set of mirrors and sent into the atmosphere coaxially aligned with the axis of the 10 cm telescope. The azimuthal scanning is carried out by rotating the whole lidar around a vertical axis (Fig. A.2). Further details on the operational principles of the lidar can be found in [22].

References

[1] Adrian RJ, Meinhart CD, et al. Vortex organization in the outer region of the turbulent boundary layer. J Fluid Mech 2000;422:1–54.
[2] Albertson JD, Kustas WP, et al. Large-eddy simulation over heterogeneous terrain with remotely sensed land surface conditions. Water Resour Res 2001;37(7):1939–53.
[3] Albertson JD, Parlange MB. Natural integration of scalar fluxes from complex terrain. Adv Water Resour 1999;23(3). 293–252.
[4] Angevine WM, Grimsdell AW, et al. Entrainment results from the Flatland boundary layer experiments. J Geophys Res-Atmos 1998;103(D12):13689–701.
[5] Bou-Zeid E, Higgins C, et al. Field study of the dynamics and modelling of subgrid-scale turbulence in a stable atmospheric surface layer over a glacier. J Fluid Mech 2010;665:480–515.
[6] Brunet Y, Finnigan JJ, et al. A wind-tunnel study of air-flow in waving wheat – single-point velocity statistics. Bound-Layer Meteorol 1994;70(1–2):95–132.
[7] Brutsaert W. Evaporation into the atmosphere. Theory, history and applications. Reidel; 1982.
[8] Bushberg JT. The essential physics of medical imaging. Lippincott Williams & Wilkins; 2002.
[9] Cohn SA, Mayor SD, et al. The lidars in flat terrain (LIFT) experiment. Bull Am Meteorol Soc 1998;79(7):1329–43.
[10] Cooney JA. Measurements on the Raman component of laser atmospheric backscatter. Appl Phys Lett 1968;12(2):40–2.
[11] Cooper DI, Eichinger WE, et al. Spatial variability of water-vapor turbulent transfer within the boundary-layer. Bound-Layer Meteorol 1992;61(4):389–405.
[12] Devara PCS. Remote sensing of atmospheric aerosols from active and passive optical techniques. Int J Remote Sens 1998;19(17):3271–88.
[13] Dupont S, Brunet Y. Coherent structures in canopy edge flow: a large-eddy simulation study. J Fluid Mech 2009;630:93–128.
[14] Eichinger WE, Cooper DI. Using lidar remote sensing for spatially resolved measurements of evaporation and other meteorological parameters. Agron J 2007;99(1):255–71.
[15] Eichinger WE, Cooper DI, et al. The development of a scanning Raman water vapor lidar for boundary layer and tropospheric observations. J Atmos Ocean Technol 1999;16(11):1753–66.
[16] Eichinger WE, Cooper DI, et al. Spatial and temporal variation in evapotranspiration using Raman lidar. Adv Water Resour 2006;29(2):369–81.
[17] Eichinger WE, Cooper DI, Parlange MB, Katul GG. The application of ascanning, water raman-lidar as a probe of the atmospheric boundary layer, IEEE. Trans.Geoscience and Remote Sensing 1993;31(1):70–9.
[18] Eichinger WE, Parlange MB, Katul GG. Lidar measurements of the dimensionless humidity gradient in an unstably stratified atmosphere. In: Lakshmi V, Albertson J, Schaake J, editors. American Geophysical Union, Models and observations of land-atmosphere interaction. 2001. p. 7-13.
[19] Finnigan J. Turbulence in plant canopies. Ann Rev Fluid Mech 2000;32:519–71.
[20] Finnigan JJ, Shaw RH. A wind-tunnel study of airflow in waving wheat: an EOF analysis of the structure of the large-eddy motion. Bound-Layer Meteorol 2000;96(1-2):211–55.
[21] Fochesatto GJ, Drobinski P, et al. Evidence of dynamical coupling between the residual layer and the developing convective boundary layer. Bound-Layer Meteorol 2001;99(3):451–64.
[22] Froidevaux M. Land-atmosphere interactions measured with Raman lidar. École Polytechnique Fédérale de Lausanne, PhD thesis, 2010.
[23] Frost R. Turbulence and diffusion in the lower atmosphere. In: Proceedings of the royal society of London series a-mathematical and physical sciences 186(1004); 1946. p. 20–35.
[24] Garai A, Kleissl J. Air and surface temperature coupling in the convective atmospheric boundary layer. J Atmos Sci 2011;68(12):2945–54.
[25] Garratt JR. The internal boundary-layer – a review. Bound-Layer Meteorol 1990;50(1–4):171–203.
[26] Goldsmith JEM, Blair FH, et al. Turn-key Raman lidar for profiling atmospheric water vapor, clouds, and aerosols. Appl Opt 1998;37(21):4979–90.
[27] Grant WB. Differential absorption and Raman lidar for water vapor profile measurements: a review. Opt Eng 1991;30(1):40–8.
[28] Higgins C, Froidevaux M, et al. The Effect of Scale on the Applicability of Taylor's Frozen Turbulence Hypothesis in the Atmospheric Boundary Layer. Bound-Layer Meteorol 2012;143(2):379–91.
[29] Higgins CW, Meneveau C, et al. Geometric alignments of the subgrid-scale force in the atmospheric boundary layer. Bound-Layer Meteorol 2009;132(1):1–9.
[30] Hua D, Liu J, et al. Daytime temperature profiling of planetary boundary layer with ultraviolet rotational Raman lidar. Jpn J Appl Phys, Part 1: Regular Papers Short Notes Rev Papers 2007;46(9A):5849–52.
[31] Jeong J, Hussain F, et al. Coherent structures near the wall in a turbulent channel flow. J Fluid Mech 1997;332:185–214.
[32] Judd MJ, Raupach MR, et al. A wind tunnel study of turbulent flow around single and multiple windbreaks .1. Velocity fields. Bound-Layer Meteorol 1996;80(1–2):127–65.
[33] Kelly M, Wyngaard JC, et al. Application of a subfilter-scale flux model over the ocean using OHATS field data. J Atmos Sci 2009;66(10):3217–25.
[34] Kleissl J, Parlange MB, et al. Field experimental study of dynamic Smagorinsky models in the atmospheric surface layer. J Atmos Sci 2004;61(18):2296–307.
[35] Koch SE, Dorian PB, et al. Structure of an internal bore and dissipating gravity current as revealed by Raman lidar. Mon Weather Rev 1991;119(4):857–87.
[36] Kollias P, Albrecht BA, et al. Radar observations of updrafts, downdrafts, and turbulence in fair-weather cumuli. J Atmos Sci 2001;58(13):1750–66.
[37] Lenshow DH, editor. Probing the atmospheric boundary layer. Boston: American Meteorological Society; 1986.
[38] Leonard DA. Observation of Raman scattering from the atmosphere using a pulsed nitrogen ultraviolet laser. Nature 1967;216:142–3.
[39] Lesieur M, Begou P, et al. Coherent-vortex dynamics in large-eddy simulations of turbulence. J Turbul 2003;4:24.
[40] Liu Z, Bromwich DH. Acoustic remote-sensing of planetary boundary-layer dynamics near Ross Island, Antarctica. J Appl Meteorol 1993;32(12):1867–82.
[41] Melfi SH, Whiteman DN. Observation of lower-atmospheric moisture structure and its evolution using a Raman lidar. Bull Am Meteorol 1985;66(10):1288–92.
[42] Neff WD. Boundary-layer research at south-pole station using acoustic remote-sensing. Antarct J Unit States 1978;13(4):179–81.
[43] Nishi A, Kikugawa H, et al. Active control of turbulence for an atmospheric boundary layer model in a wind tunnel. J Wind Eng Ind Aerodyn 1999;83:409–19.
[44] Parlange MB, Eichinger WE, et al. Regional-scale evaporation and the atmospheric boundary-layer. Rev Geophys 1995;33(1):99–124.
[45] Parlange MB, Albertson JD, Eichinger WE, Cahill AT. Evaporation: use of fast response turbulence sensors, raman lidar and passive microwave remote sensing. In: Parlange MB, Hopmans JW, editors. Vadose zone hydrology: cutting across disciplines. Oxford University Press; 1999. p. 260–278.
[46] Parlange MB, Brutsaert W. Are radiosonde time scales appropriate to characterize boundary layer wind profiles? J Appl Meteorolo 1990;29:249–55.
[47] Patton EG, Shaw RH, et al. Large-eddy simulation of windbreak flow. Bound-Layer Meteorol 1998;87(2):275–306.
[48] Pinzon JE, Puente CE, et al. A multifractal analysis of lidar measured water vapour. Bound-Layer Meteorol 1995;76(4):323–47.
[49] Porte-Agel F, Meneveau C, et al. A scale-dependent dynamic model for large-eddy simulation: application to a neutral atmospheric boundary layer. J Fluid Mech 2000;415:261–84.
[50] Renaut D, Pourny JC, et al. Day-time Raman-lidar measurements of water vapor. Opt Lett 1980;5(6):233–5.
[51] Ristori PR. Development of a high spatial and temporal resolution Raman lidar for turbulent observations. Ecole Polytechnique Fédérale de Lausanne, PhD thesis, 2007.
[52] Ristori PR, Froidevaux M. et al. Development of a temperature and water vapor Raman LIDAR for turbulent observations. In: Proceedings of SPIE – the international society for optical engineering, 2005.
[53] Schmid HP. Source areas for scalars and scalar fluxes. Bound-Layer Meteorol 1994;67(3):293–318.
[54] Schneider K, Farge M, et al. Coherent vortex simulation of three-dimensional turbulent mixing layers using orthogonal wavelets. J Fluid Mech 2005;534:39–66.
[55] Senff C, Bosenberg J, et al. Measurements of water-vapor flux profiles in the convective boundary-layer with lidar and radar-RASS. J Atmos Ocean Technol 1994;11(1):85–93.
[56] Serikov I. Ristori P. et al. Temperature and water vapor Raman lidar for observation of land-atmosphere interactions. In: 23rd international laser radar conference, Nara, Japan, 2006.
[57] Shaw RH, Schumann U. Large-eddy simulation of turbulent-flow above and within a forest. Bound-Layer Meteorol 1992;61(1-2):47–64.
[58] Sutton GC. Wind structure and evaporation in a turbulent atmosphere. In: Proceedings of the royal society of london series a-mathematical and physical sciences 146(A858) 1934. p. 0701–722.
[59] Tong CN, Wyngaard JC, et al. Experimental study of the subgrid-scale stresses in the atmospheric surface layer. J Atmos Sci 1999;56(14):2277–92.
[60] Tratt DM, Whiteman DN, et al. Active Raman sounding of the earth's water vapor field. Spectrochimica Acta Part A 2005;61:2335–41.
[61] Turner DD, Ferrare RA, et al. Automated retrievals of water vapor and aerosol profiles from an operational Raman lidar. J Atmos Ocean Technol 2002;19(1):37–50.
[62] Vaughan G, Wareing DP, et al. Humidity measurements in the free troposphere using Raman backscatter. Quart J – Roy Meteor Soc 1988;114(484):1471–84.

[63] Waleffe F. On a self-sustaining process in shear flows. Phys Fluids 1997;9(4):883–900.
[64] Watanabe T. Large-eddy simulation of coherent turbulence structures associated with scalar ramps over plant canopies. Bound-Layer Meteorol 2004;112(2):307–41.
[65] Weitkamp C. Lidar: range-resolved optical remote sensing of the atmosphere. Springer Science + Business Media; 2005.
[66] Whiteman DN, Demoz B, et al. Raman lidar measurements during the international H_2O project. Part II: Case studies. J Atm Ocean Technol 2006;23(2):170–83.
[67] Whiteman DN, Melfi SH, et al. Raman lidar system for the measurement of water vapor and aerosols in the Earth's atmosphere. Appl Opt 1992;31(16):3068–82.
[68] Wilczak JM, Gossard EE, et al. Ground-based remote sensing of the atmospheric boundary layer: 25 years of progress. Bound-Layer Meteorol 1996;78(3–4):321–49.
[69] Yang B, Raupach MR, et al. Large-eddy simulation of turbulent flow across a forest edge. Part I: Flow statistics. Bound-Layer Meteorol 2006;120(3):377–412.